Supporting Information

Experimental Section

***Materials*:**

The following chemicals were used as received without further purification: PVDF-HFP (average Mw ~455,000, average Mn ~110,000, pellets) was purchased from Sigma-Aldrich; N, N-dimethylformamide (DMF, analytical grade, 99.9%) was purchased from Aladdin; TiO_2 (TO) and $BaTiO_3$ (BTO) nanoparticles were purchased from Aladdin; Nano ($Li_{6.4}La_3Zr_{1.4}Ta_{0.6}O_{12}$) LLZTO particles were supplied by Guangzhou Fangzhen Science and Technology Co., Ltd. $BaCl_2$ Propylene Carbonate (PC, 99%, Aladdin), N-methyl-2-pyrrolidone (NMP, 99.9%, Aladdin), and lithium bis((trifluoromethyl)sulfonyl) azanide (LiTFSI, 99.9%, Macklin), were vacuum-dried at 120 °C for 24 hours before use and then transferred to the glove box for storage (Ar atmosphere, H_2O and O_2 less than 0.1 ppm). Commercially available $LiFePO_4$ (LFP), $LiNi_{0.8}Co_{0.1}Mn_{0.1}O_2$ (NCM811), super-P, and polyvinylidene difluoride (PVDF) were purchased from Canrud. Barium chloride ($BaCl_2$) was purchased from Xiya Chemical. Strontium chloride ($SrCl_2$, AR grade, 99.5%), titanium tetrachloride ($TiCl_4$, 99.9%, metals basis), and poly(vinyl pyrrolidone) (PVP, average molecular weight ~10,000) were obtained from Aladdin. Potassium hydroxide (KOH, 95%) was supplied by Macklin. All chemicals were used as received without further purification.

$Sr_{0.3}Ba_{0.7}TiO_3$ (BST) preparation

Different proportions of $BaCl_2 \cdot 2H_2O$ and $SrCl_2 \cdot 6H_2O$ were dissolved in deionized water and magnetically stirred. Polyvinylpyrrolidone (PVP, Mw ≈ 10,000) was then added, and stirring continued until the solution became clear. Subsequently, $TiCl_4$ solution (3.84 mol L^{-1}) was slowly added dropwise to the mixture; no color change occurred during this process. In another beaker, KOH was dissolved in deionized water to prepare a KOH solution. After the precursor solution became homogeneous, it was transferred to a three-necked flask equipped with a condenser, and KOH solution was slowly added dropwise through a dropping funnel/syringe with continuous stirring, resulting in a white precipitate. The suspension was heated to 90 °C and reacted for 3 hours. After cooling to room temperature, the precipitate was collected and washed with

deionized water. The following cycle was repeated: deionized water was added, stirring for 10 minutes, allowing to stand for separation, and the supernatant was decanted. Repeat this washing cycle 6 times until no white precipitate forms after adding $AgNO_3$ solution to the supernatant, and the supernatant pH is close to neutral. Dry the washed powder in an oven at 120 °C and gently grind it. Finally, calcine the dried precursor powder in air at 800 °C for 3 hours (heating rate 5 °C min^{-1}) to obtain BST nanoparticles with different Ba/Sr ratios.

Note: $TiCl_4$ is sensitive to moisture and highly corrosive; it should be added in a fume hood with appropriate personal protective equipment worn. The dissolution of KOH is a strongly exothermic reaction; an ice-water bath should be used during the dropwise addition.

Electrode preparation

Preparation of LFP electrode and the Li||LFP cell assembly

Commercial LFP, Super-P, and PVDF were mixed in a mass ratio of 8:1:1 in NMP to form a uniform slurry, which was then coated onto carbon-coated aluminum foil. The prepared electrodes were vacuum-dried at 80 °C for 24 hours prior to battery assembly. The active material loading on the LFP cathode was approximately 2 mg cm^{-2} and 3.2 mg cm^{-2}. Subsequently, different PVDF-HFP-based electrolytes were sandwiched between the LFP cathode and the lithium metal anode to assemble Li||LFP batteries. Electrochemical tests on these batteries were conducted at room temperature within a voltage range of 2.5-3.8 V, corresponding to the theoretical capacity of the LFP cathode (170 mAh g^{-1}). Before testing, the electrolyte film was activated by quickly immersing it in a 1 M LiTFSI solution in propylene carbonate (PC) for 3-5 s, then the surface solvent was absorbed with lint-free paper. The electrolyte film's weight increased by approximately 8 mg. To improve the interface, 5.5 μL of liquid electrolyte—1 M LiPF6 in a mixture of ethylene carbonate, dimethyl carbonate, and ethyl methyl carbonate (EC: DMC: EMC = 1:1:1 vol%)—was applied to both the lithium foil and electrode sheets during assembly. This electrolyte primarily enhances electrode/electrolyte interfacial wettability and ensures reliable electrochemical contact. The amount of

electrolyte was precisely controlled using a calibrated micropipette to maintain consistency across all cells.

Preparation of NCM811 cathode and the Li||NCM811 cell assembly:

Commercial NCM811, Super-P, and PVDF were combined in a mass ratio of 8:1:1 using NMP to form a consistent slurry, which was then coated onto carbon-coated aluminum foil. The electrode films were vacuum-dried at 80 °C for 24 hours before assembling the batteries. The active material loading on the NCM811 cathode was approximately 1.3 mg cm^{-2}. Finally, various PVDF-HFP-based electrolytes were placed between the NCM811 cathode and the lithium metal anode to assemble Li||NCM811 batteries. These batteries underwent electrochemical testing at room temperature, with a voltage window of 3.0-4.3 V, matching the theoretical capacity of 180 mAh g^{-1} for NCM811.

Fabrication of CPE.

The precursor solution for the polymer membrane was prepared inside an argon-filled glove box. The process began by mixing 1 g of PVDF-HFP, 1 g of LiTFSI, and 7.5 mL of DMF, then stirring the mixture at 80 °C for 3 to 4 hours to produce Solution A. Meanwhile, 0.1 g of LLZTO and varying amounts of dielectric powder were added to 2.5 mL of DMF and sonicated for 1 hour, with temperature monitored to avoid overheating. Solutions A and B were then combined in the glove box and stirred for an additional 5 hours to create the final precursor solution. Membranes with 10 wt.% LLZTO and 3 wt.% TO were labeled PLT; those with 10 wt.% LLZTO and 3 wt.% BTO were labeled PLBT; and those with 10 wt.% LLZTO and 3 wt.% BST were labeled PLBST. Finally, the solution was poured onto a glass plate and dried by infrared heating at 100 °C for 3.5 hours. The electrolyte membrane was then cut into sheets suitable for battery assembly.

Materials Characterization:

X-ray diffraction (XRD, Rigaku Smartlab) was conducted at room temperature using a Cu-Kα X-ray source (λ = 1.5418 Å) over a scan range of 5° to 80° to analyze the crystallographic structure of the electrolyte membrane. Field-emission scanning electron microscopy (FEG-SEM; Hitachi SU-8230) examined the morphology, particle

distribution, and cross-section of the membrane. Energy-dispersive spectroscopy (EDS, Bruker) mapping mapped the element distribution of C, O, F, S, N, Sr, La, Zr, and Ti. Infrared spectra were recorded with a Fourier transform infrared spectrometer (FTIR, PerkinElmer Frontier FTIR with UATR), covering 650–4000 cm^{-1}. X-ray photoelectron spectroscopy (XPS; Thermo Scientific) used an ESCALAB 250Xi instrument, referencing binding energies to the C 1s peak at 284.8 eV and processed with Thermo Avantage software. Thermogravimetric analysis (TGA, NETZSCH TG209F1) tracked mass loss during heating at 10 °C min-1 in N2 from 30 °C to 800 °C. Tensile tests were performed with a universal testing machine (ZwickRoell 500 N zwickiLine). Sample strips (2 cm × 8 cm) prepared in a glove box were wrapped in cling film and then tested outside the glove box. Raman spectra were obtained at room temperature using a Thermo Scientific DXRXI system with 532 nm Ar laser excitation. The dielectric properties of the membrane were measured with a broadband dielectric impedance spectrometer (Novocontrol Concepts 50). Surface examination involved Kelvin probe force microscopy (KPFM) via atomic force microscopy. The dielectric properties of the samples were examined by piezoelectric force microscopy (PFM). (Bruker Dimension Icon, Germany). Lithium metal samples were transferred in an argon-filled sealed container to prevent contamination from ambient oxygen and moisture during SEM and XPS analyses.

Battery assembly and measurement:

The Neware BTS charge and discharge system was employed to evaluate the cycling stability of the electrolyte membrane in relation to the lithium metal anode using Li symmetric cells at various current densities. The cycling performance and rate capability of the cells (Li||LFP and Li||NCM811) were also assessed.

Electrochemical measurements：

All Gel Polymer Electrolyte coin cells were assembled using CR2032 coin cells within an argon-filled glove box. Linear sweep voltammetry (LSV) tests were performed on Li||stainless steel (SS) cells at a scan rate of 0.5 mV s-1, ranging from 2 to 7 V at room temperature, to evaluate electrolyte stability. The electrolyte membrane's

performance was tested on Li||Li cells with an IVIUMnSTAT device at room temperature, and relevant parameters were computed following Eq. (1).(1).

$$t_{Li^+} = \frac{I_s R_S(\Delta V - I_0 R_0)}{I_0 R_0(\Delta V - I_s R_s)} \#(1)$$

ΔV represents the potential polarization difference (0.01 V), with R0 and Rs being the interfacial resistances of the battery prior to and following polarization. I0 and Is denote the currents before and after polarization. Conductivity (σ) testing was carried out on SS||SS cells and determined using Equation (2).(2).

$$\sigma = \frac{d}{R_\beta S} \#(2)$$

Where **d** and **S** represent the thickness of the electrolyte membrane and the contact area of the cell, respectively, $\mathbf{R_\beta}$ is the resistance of the electrolyte membrane, and **σ** is the ionic conductivity ($S \cdot cm^{-1}$).

The activation energy (E_a) of CPEs (Composite Polymer Electrolytes) can be determined using the Arrhenius equation:

$$\sigma(T) = A\exp\frac{-E_a}{RT} \#(3)$$

Where E_a is the activation energy, **A** is the pre-exponential factor, **R** is the thermodynamic constant, and **T** represents the testing temperature. The temperature range is from 25 °C to 60 °C with a step size of 5 °C, and the frequency range is from 10^6 to 0.1 Hz. The sample's bulk resistance is calculated based on the EIS curve.

IVIUMnSTAT was used for the above experimental process.

Computational Method:

Li-TFSI Binding Energy Calculation:

To rationalize how local dielectric microenvironments influence LiTFSI dissociation, we calculated the Li-TFSI binding energies within three continuum environments. The macroscopic effective dielectric constants used as key parameters in the simulation were directly obtained from Broadband Dielectric Spectroscopy measurements at room temperature (as shown in **Figure 3a**). No explicit polymer chains were included; instead, an implicit SMD continuum was employed to isolate the dielectric effect,

avoiding reliance on arbitrary oligomer conformations. This approach makes the comparison relative and mechanistic, rather than absolute.

Geometry optimizations and harmonic frequency calculations were conducted using Gaussian 16 Rev. C.01 at the B3LYP-D3(BJ)/6-311+G(d,p) level with the SMD solvation model. The reported binding energies are ZPE-corrected electronic interaction energies, defined as

$$E_{bind} = E_{complex} - \left(E_{Li+} + E_{TFSI-}\right) \#(4)$$

with Li^+ and $TFSI^-$ evaluated in the *same* continuum environment.

For robustness, we cross-checked the PLT, PLBT, and PLBST cases with PBE0-D3(BJ) single points on the B3LYP-optimized geometries; the qualitative trend (PLT > PLBT > PLBST in $|E_{bind}|$) remained unchanged.

ESP Calculation:

First-principles density functional theory (DFT) calculations were performed to systematically investigate the surface electrostatic potentials of anatase TO, BTO, and BST. All calculations were carried out using the Vienna *Ab initio* Simulation Package (VASP) with the Perdew–Burke–Ernzerhof (PBE) functional within the generalized gradient approximation (GGA).

Bulk structures of TO and BTO were fully relaxed with simultaneous optimization of atomic positions, cell shape, and cell volume. Based on the optimized BTO structure, a 2 × 2 × 2 supercell was constructed, and Sr was substituted at Ba sites (Ba:Sr = 6:2) to approximate the BST composition, followed by full structural relaxation of the substituted model (one representative configuration).

Surface slab models were then built from the optimized bulk structures: the anatase TO (101) surface and the (001) surfaces of BTO and BST. During slab relaxation, only the top two atomic layers were allowed to relax while the remaining layers were fixed to mimic the bulk constraint. After relaxation, single-point calculations were performed to obtain the electrostatic potential distributions on the relaxed surfaces (extracted from the LOCPOT file). Dipole corrections were applied along the surface normal (LDIPOL

= .TRUE., IDIPOL = 3). Van der Waals interactions were included using a dispersion-corrected scheme (IVDW).

The k-point meshes for the TO, BTO, and BST surface models were set to 5 × 7 × 1, 6 × 6 × 1, and 3 × 3 × 1, respectively. The plane-wave cutoff energy was 500 eV for all calculations. Structural relaxations were converged to an electronic energy tolerance of 1×10^{-5} eV, with residual atomic forces below 0.05 eV $Å^{-1}$. For the final single-point calculations, a tighter electronic convergence criterion of 1×10^{-6} eV was used.

COMSOL Simulation

The finite element analysis simulations are performed using COMSOL Multiphysics. The simulation considers three different material models (PLT, PLBT, PLBST). The initial ion concentration is set to 1000 mol/m³. The simulation region is 110 × 70 μm. During the simulation, ions enter from the top surface and exit from the bottom surface. Due to differences in electrolyte tortuosity, variations in ion and electric field distributions occur. Additionally, a current-density boundary condition related to ion concentration is specified at the upper surface, while a uniform potential (0 V) is applied at the lower surface. The specific parameters used in this mode are listed below:

Theoretical method

The primary equation solved in the simulation is derived from the conservation of electric charge and the constitutive material relationship.

a) Charge Conservation Equation (Steady-State):

$$\nabla \cdot J = 0 \#(5)$$

∇ : The divergence operator.

J : The current density vector (unit: A/m^2).

b) Constitutive Relation (Ohm's Law):

$$J = \sigma \cdot E \#（6）$$

σ : The electrical conductivity of the material (unit: S/m).

E: The electric field intensity vector (unit: V/m).

c) Electric Field Definition:

$$E = \nabla V \#（7）$$

V: The electric potential or voltage (unit: Volts, V).

∇: The gradient operator. The electric field is the negative gradient of the electric potential.

By substituting Ohm's Law and the electric field definition into the charge conservation equation, we get the primary equation that the simulation solver computes:

$$\nabla \cdot (\sigma \nabla V) = 0 \#（8）$$

d) Transport of Diluted Species Equation

$$\frac{\partial c_i}{\partial t} + \nabla \cdot \left(- D_i \nabla c_i \right) + u \cdot \nabla c_i = R_i \#（9）$$

c_i: Molar concentration of species

t : Time

D_i: Diffusion coefficient of species i

R_i: Reaction rate term for species i(source/sink)

By solving the above equations, the distribution of electric potential and concentration distribution can be obtained.

Table S1. List of ingredients used for the preparation of CPEs.

	Filler type	LLZTO/g	PVDF-HFP/g	LiTFSI/g	DMF/ml
PLT	0.03 g TO	0.10	1.00	1.00	10
PLBT	0.03 g BTO	0.10	1.00	1.00	10
PLBST	0.03 g BST	0.10	1.00	1.00	10

Table S2. Physical Formulations and total liquid phase content of the PLBST electrolyte.

	Mass of the dry membrane/mg	Mass of the membrane with PC/mg	Retention/mg	Content/wt%
1	39.2	47.4	8.2	0.172995781
2	27.6	36.2	8.6	0.237569061
3	23.7	31.8	8.1	0.254716981
4	30.3	39.5	9.2	0.232911392
5	37.1	45.2	8.1	0.17920354
6	25.1	33.8	8.7	0.25739645
7	25.4	32.7	7.3	0.22324159
8	27.8	36.1	8.3	0.229916898
9	35	45.5	10.5	0.230769231
10	34.2	44.8	10.6	0.236607143
11	33	40.4	7.4	0.183168317
12	32	42.3	10.3	0.243498818
Avg	30.86666667	39.64166667	8.775	0.2234996

The standard density of commercial liquid electrolytes is 1.25 g cm^{-3}, so the mass of the wetting agent is calculated as follows:

$M_{LE} = 11\ \mu L \cdot 1.25\ mg\ \mu L^{-1} = 13.75\ mg\#$（10）

Calculated using the mean values of the component weights to determine the final liquid mass percentage:

$$W_{liquid} = \frac{8.775 + 13.75}{8.775 + 13.75 + 30.867} \cdot 100\% = 42.19\ wt\%\ \#(11)$$

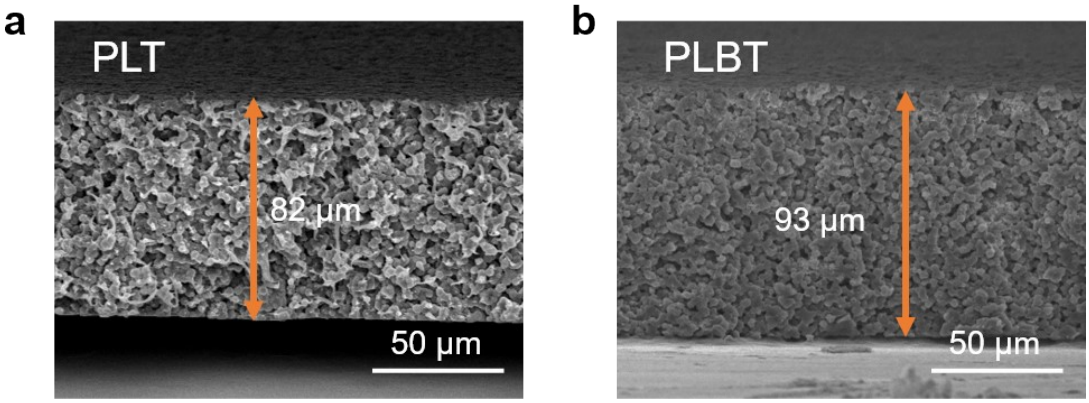

Figure S1. Cross-sectional SEM images of the PLT (a), PLBT (b).

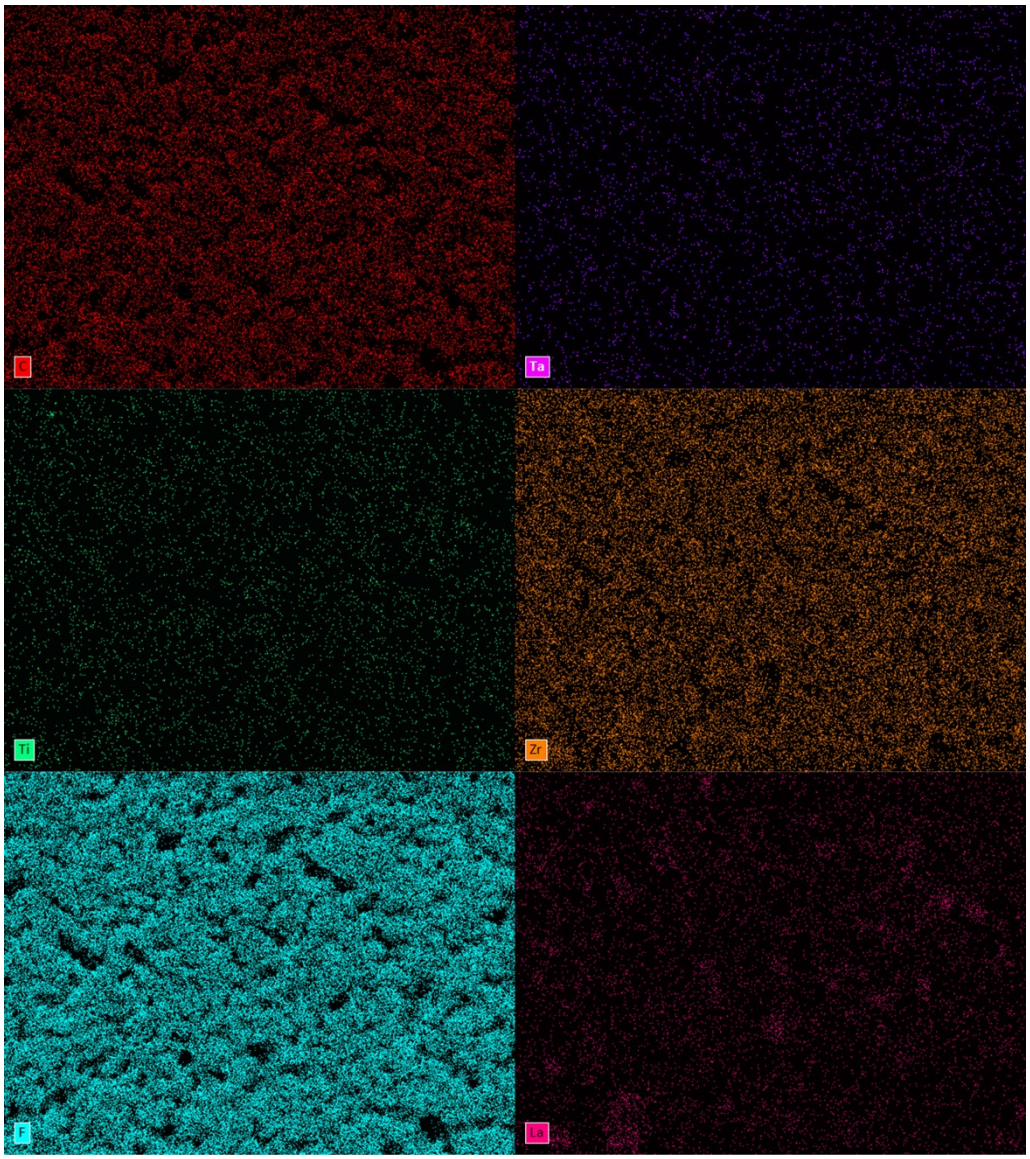

Figure S2. Elemental mapping of C, F, Ta, Zr, La and Ti in PLT via EDS.

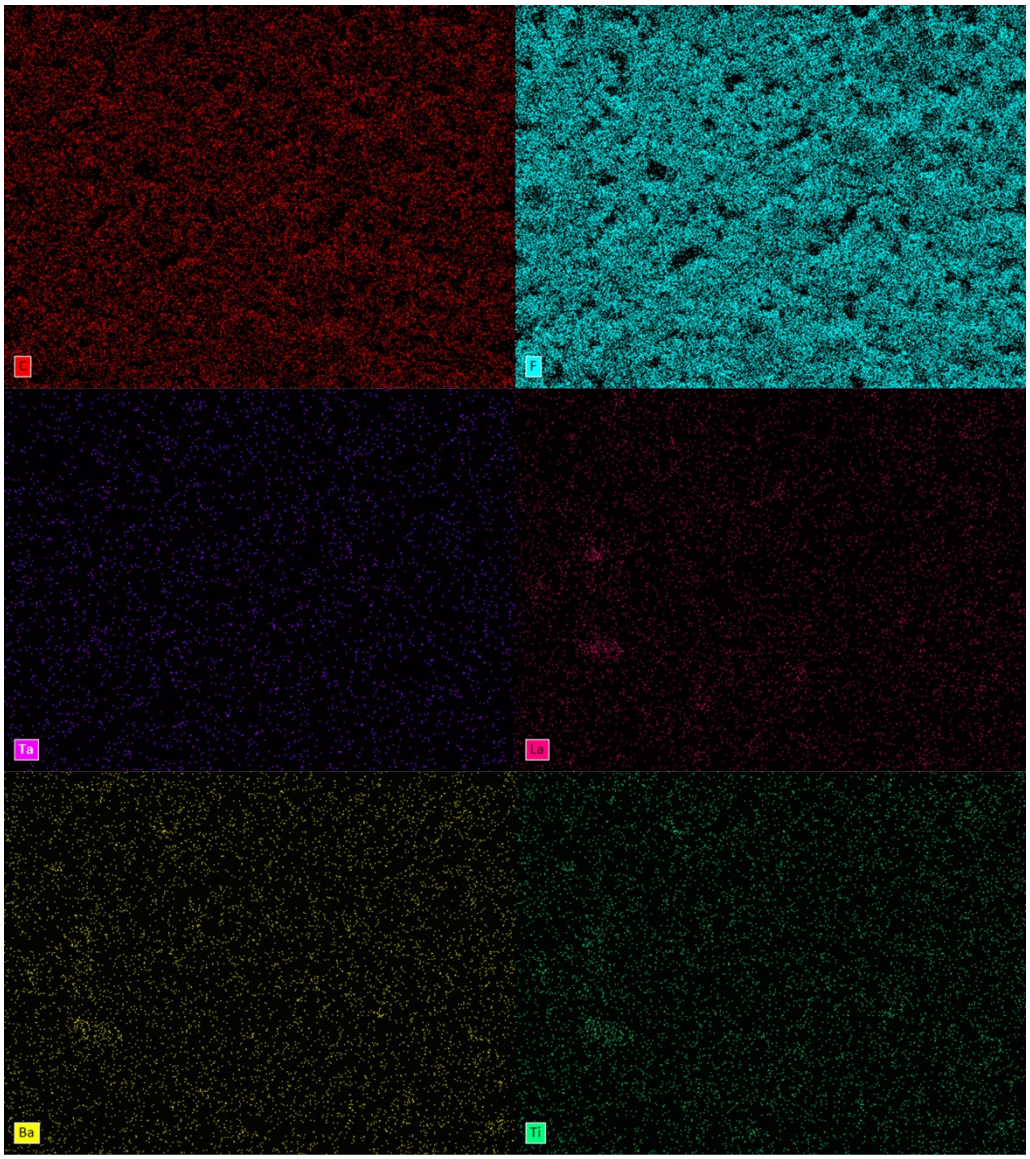

Figure S3. Elemental mapping of C, F, Ta, Ba, La, and Ti in PLBT via EDS.

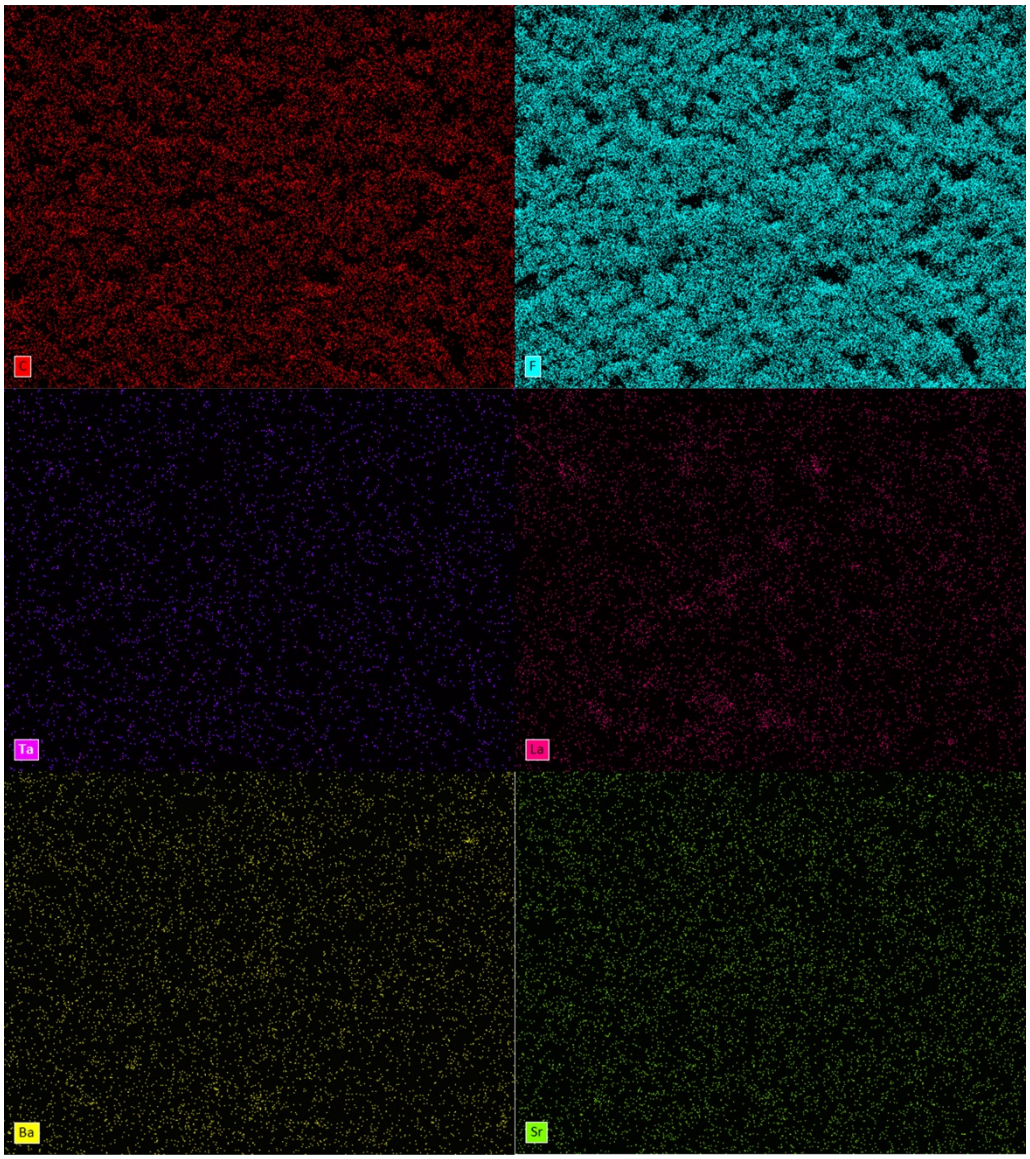

Figure S4. Elemental mapping of C, F, Ta, Ba, La, and Sr in PLBT via EDS

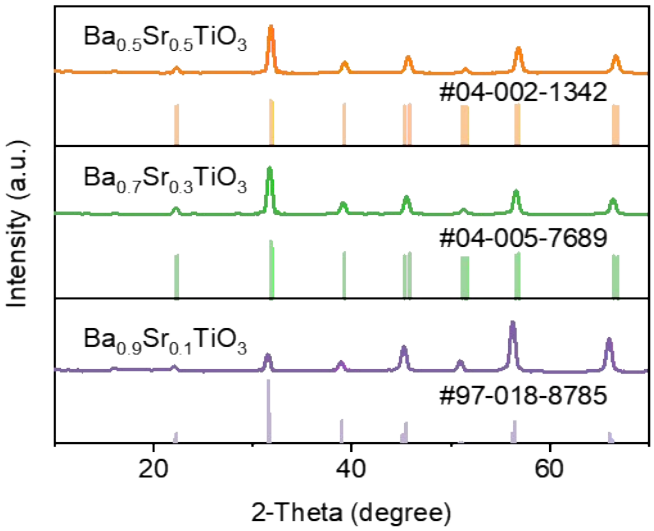

Figure S5. XRD patterns of BST with different Ba/Sr ratios.

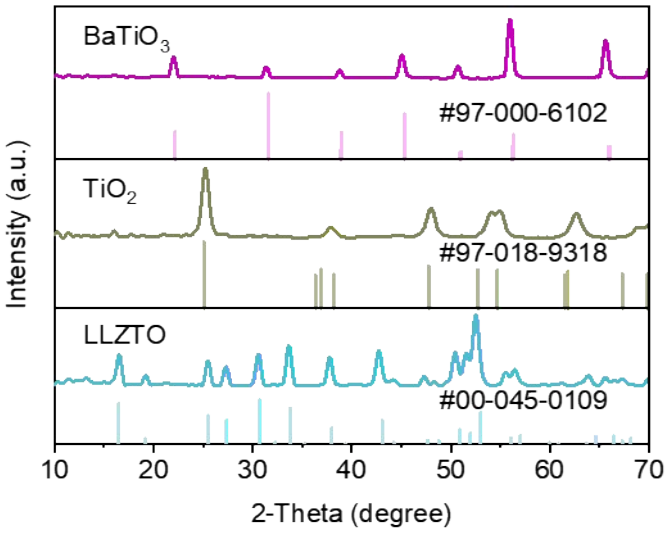

Figure S6. XRD patterns of LLZTO, TO, and BTO.

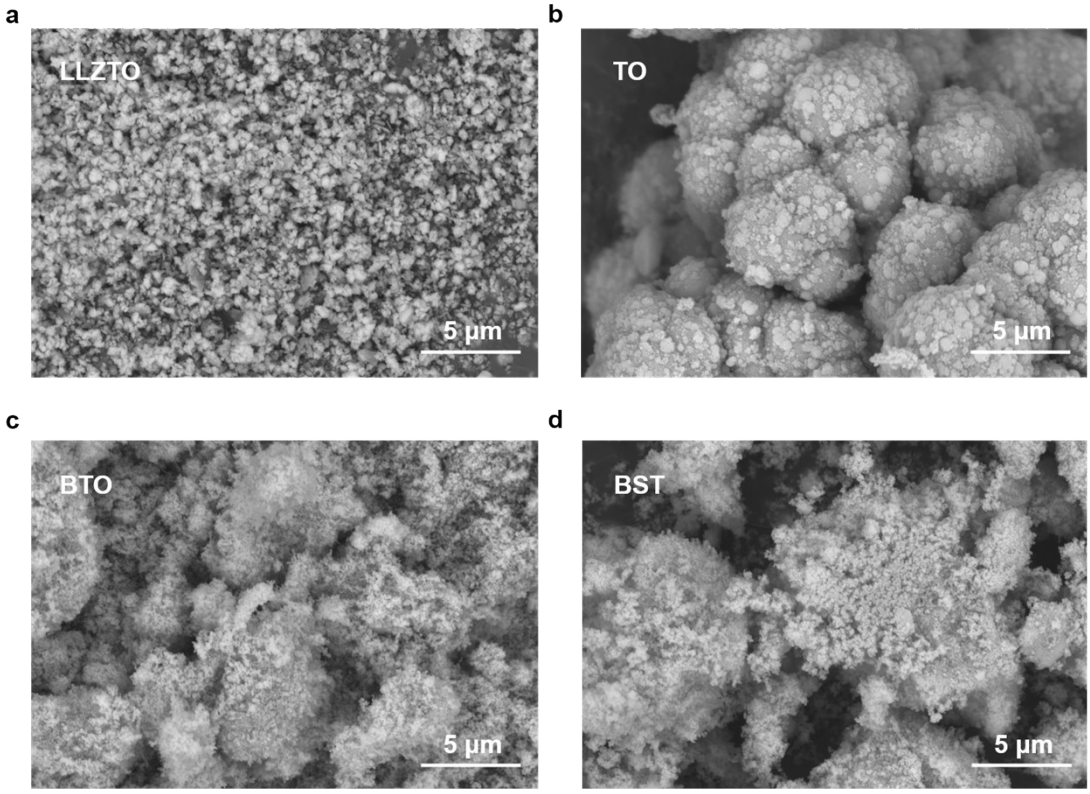

Figure S7. SEM images of the LLZTO, TO, BTO, and BST.

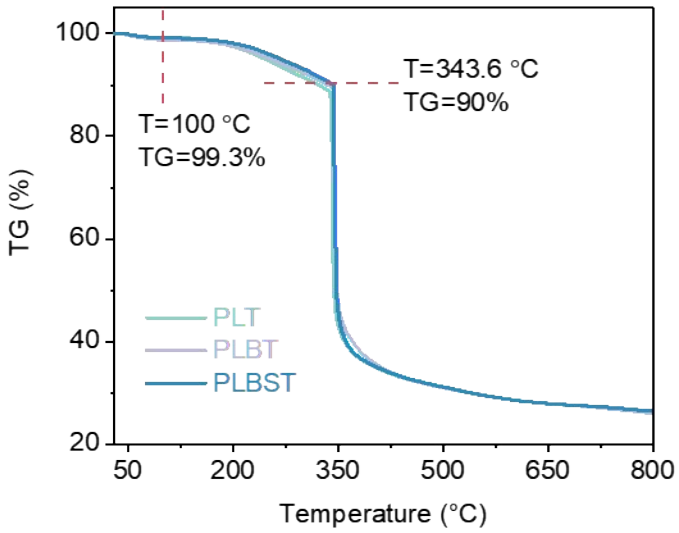

Figure S8. TGA curves of CPEs with no PC.

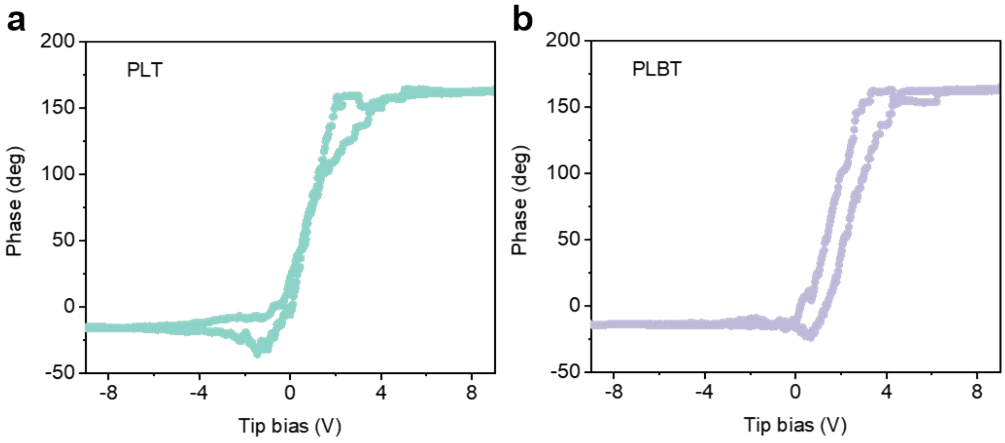

Figure S9. Hysteresis loop obtained from piezoelectric force microscopy analysis of (a) PLT and (b) PLBT electrolyte.

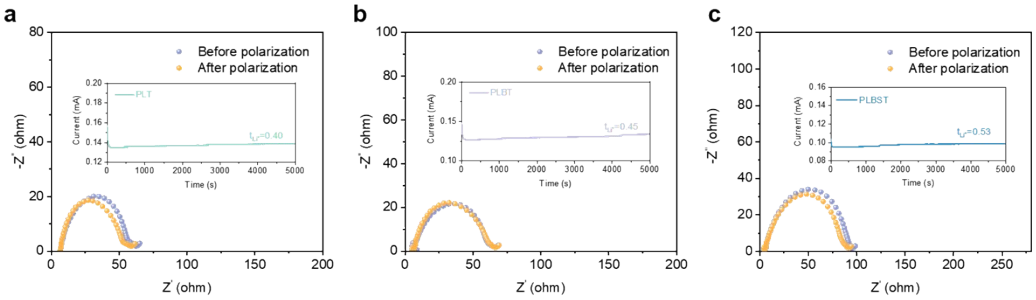

Figure S10. The t_{Li^+} of (a) PLT, (b) PLBT and (c) PLBST.

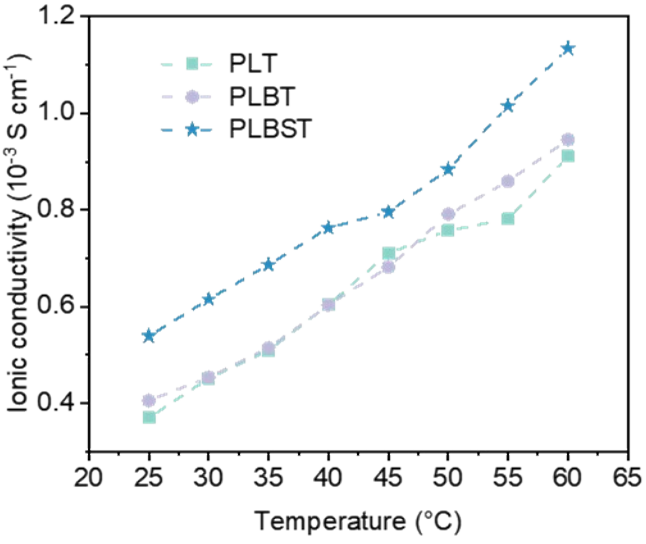

Figure S11. Temperature-dependent ionic conductivity of CPEs.

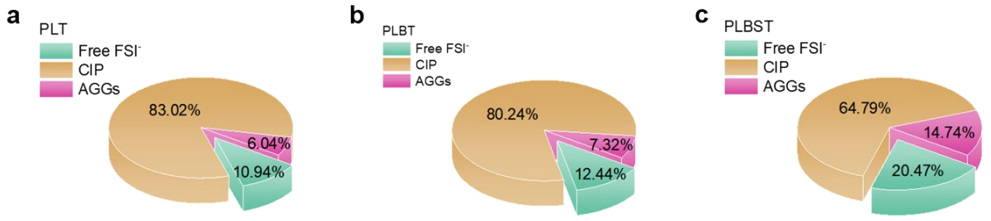

Figure S12. Corresponding quantification of $TFSI^-$ anion states in electrolyte Raman spectra.

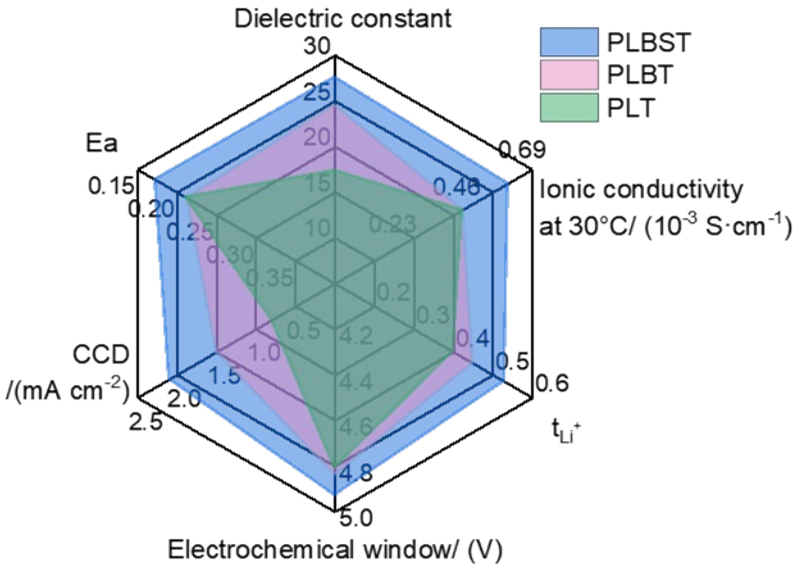

Figure S13. Performance radar plot of the electrolytes.

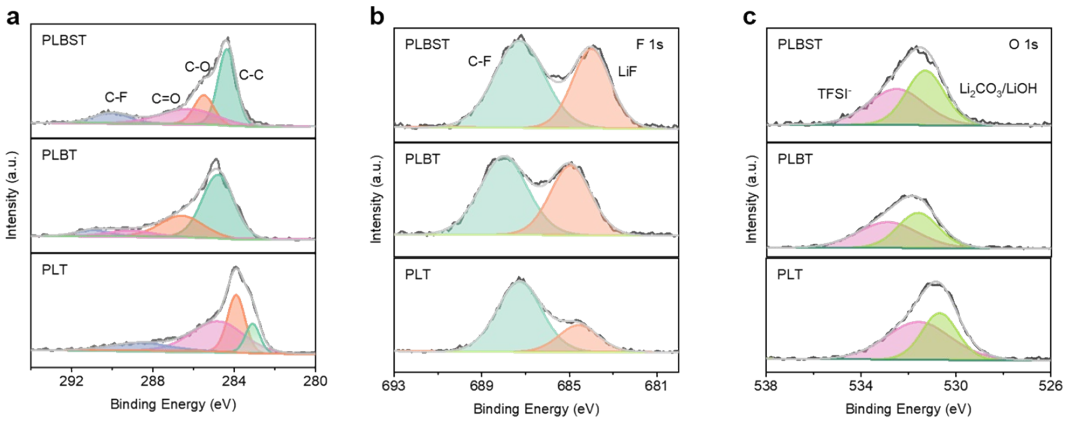

Figure S14. XPS spectra for (a) C 1s, (b) F 1s, and (c) O 1s of NCM811 cathodes after the rate test.

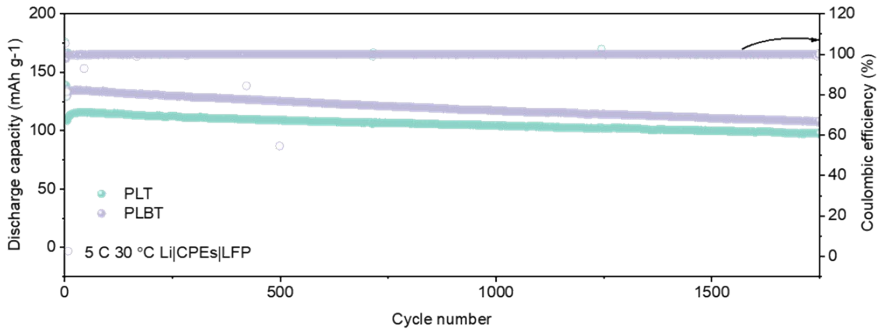

Figure S15. Long-term cycling performance of Li| CPEs |LFP at 5 C at 30 °C.

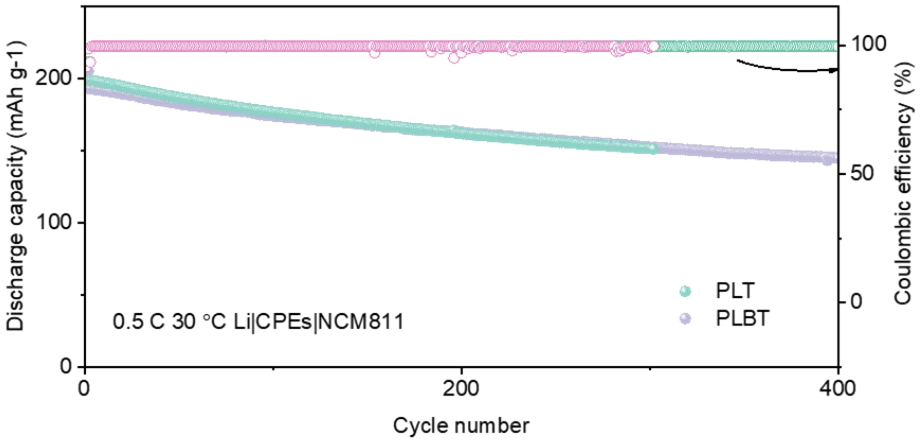

Figure S16. High-rate cycling performance of Li| CPEs |NCM811 at 30 °C.

Table S3 The property comparisons of this work with other CPEs.

CPEs	t_{Li^+}	LSV (V)	CCD (mA·cm^{-2})	Li||Li cells at RT	Cycling Performance at RT	Ref.
P(VDF CTFE)/LLZTO-PAA	0.336	4.5	0.6	0.1mA·cm^{-2} for 3500 h	LFP:1C,650th,91.45%	[1]
Ti@LLZTO/PVDF-HFP	0.48	4.75	/	0.1mA·cm^{-2} and 0.1mAh·cm^{-2} for 1550 h	LFP:0.5C,100th,95.5% NCM811:1C,100th,66%	[2]
PVDF/LATP	0.58	4.5	2.2	0.5mA·cm^{-2} and 0.5mAh·cm^{-2} for 600 h	NCM811:0.5C,150th,91.5%	[3]
PVDF/CuPcLi	0.74	4.8	1.9	0.2mA·cm^{-2} for 2000 h	NCM622:1C,300th,88%	[4]
LiDFOB-BTO/PVDF	0.70	4.75	2.4	0.2mA·cm^{-2} and 0.1mAh·cm^{-2} for 5000 h	LFP:2C,1000th,82.7% NCM811:1C,300th,71.1%	[5]
LSTO/PVDF-HFP	0.66	4.7	1.9	0.2mA·cm^{-2} and 0.1mAh·cm^{-2} for 480 h	LFP:1C,130th:88.7% NCM811:0.5C,200th:70.7%	[6]
NaNbO3/PVDF	0.49	4.7	2.58	0.1mA·cm^{-2} and 0.1mAh·cm^{-2} for 2800 h	NCM811:2C,2200th:60%	[7]
La2O3/PVDF-HFP	0.54	4.5	2.3	0.1mA·cm^{-2} and 0.1mAh·cm^{-2} for 500 h	LFP:0.4C,180th:99.5%	[8]
MOF@GF-PVDF-HFP	0.56	4.7	0.56	0.1mA·cm^{-2} and 0.1mAh·cm^{-2} for 2000 h	LFP:2C,800th:93.1% NCM811:0.5C,200th:89.3%	[9]
HKUST@PI/PVDF	0.56	4.5	/	0.1mA·cm^{-2} and 0.1mAh·cm^{-2} for 900 h	NCM:0.2C,500th:86%	[10]
PEO/UiO-66	0.36	5	/	0.1mA·cm^{-2} and 0.1mAh·cm^{-2}	LFP:1C,100th:98.45% (60°C)	[11]

				for 350 h (60°C)		
Ga/NbLLZO/BTO/PVDF	0.41	4.95	1.5	0.2mA·cm^{-2} and 0.2mAh·cm^{-2} for 2000 h	LFP:2C,1000th:70% NCM811:2C,700th:81%	[12]
LPPO-PVDF	0.47	4.8	/	0.1mA·cm^{-2} for 1400 h	NCM811:1C,1500th:70.9%	[13]
PPU-Zr	0.55	5.5	2.6	0.1mA·cm^{-2} and 0.1mAh·cm^{-2} for 4000 h	NCM811:3C,500th:81.3%	[14]
PLP-60LLZTO-SN	0.6	4.7	/	0.1mA·cm^{-2} for 500 h	LFP:0.2C,100th:83.5% NCM811:0.2C,100th:65%	[15]
STO/LLZTO/PVDF-HFP	0.51	4.8	2.2	0.1mA·cm^{-2} and 0.1mAh·cm^{-2} for 1900 h	LFP:5C,1200th:97% NCM811:5C,300th:72.2%	[16]
PLBST	**0.53**	**4.93**	**2.1**	**0.3mA·cm^{-2} and 0.3mAh·cm^{-2} for 1900 h**	LFP:5C,1500th:97.3% **NCM811:0.5C,800th:70.75%**	**This work**

Reference

[1] X. An, Y. Liu, K. Yang, J. Mi, J. Ma, D. Zhang, L. Chen, X. Liu, S. Guo, Y. Li, Y. Ma, M. Liu, Y. He, F. Kang, Dielectric filler-induced hybrid interphase enabling robust solid-state li metal batteries at high areal capacity, Advanced Materials 36 (2024) 2311195. https://doi.org/10.1002/adma.202311195.

[2] T. Duan, H. Cheng, Q. Sun, Y. Liu, W. Nie, Y. Chu, Q. Xu, X. Lu, Reinforcing interfacial compatibility of LLZTO/PVDF-HFP composite electrolytes by chemical interaction for solid-state lithium metal batteries, Journal of Power Sources 589 (2024) 233789. https://doi.org/10.1016/j.jpowsour.2023.233789.

[3] K. Yang, L. Chen, J. Ma, C. Lai, Y. Huang, J. Mi, J. Biao, D. Zhang, P. Shi, H. Xia, G. Zhong, F. Kang, Y. He, Stable interface chemistry and multiple ion transport of composite electrolyte contribute to ultra-long cycling solid-state $LiNi_{0.8}$ $Co_{0.1}$ $Mn_{0.1}$ O_2 /lithium metal batteries, Angew Chem Int Ed 60 (2021) 24668–24675. https://doi.org/10.1002/anie.202110917.

[4] H. Wang, H. Cheng, D. Li, F. Li, Y. Wei, K. Huang, B. Jiang, H. Xu, Y. Huang, Lithiated copper polyphthalocyanine with extended π-conjugation induces LiF-rich solid electrolyte interphase toward long-life solid-state lithium-metal batteries, Advanced Energy Materials 13 (2023) 2204425. https://doi.org/10.1002/aenm.202204425.

[5] Y. Zhang, H. Liu, F. Liu, S. Zhang, M. Zhou, Y. Liao, Y. Wei, W. Dong, T. Li, C. Liu, Q. Liu, H. Xu, G. Sun, Z. Wang, Y. Ren, J. Yang, Dual-anion-rich polymer electrolytes for high-voltage solid-state lithium metal batteries, ACS Nano 19 (2025) 3197–3209. https://doi.org/10.1021/acsnano.4c09953.

[6] Y. Liao, X. Wang, H. Yuan, Y. Li, C. Xu, S. Li, J. Hu, S. Yang, F. Deng, J. Liu, J. Huang, Ultrafast li-rich transport in composite solid-state electrolytes, Advanced Materials (2025) 2419782. https://doi.org/10.1002/adma.202419782.

[7] X. An, Y. Liu, K. Yang, J. Mi, J. Ma, D. Zhang, L. Chen, X. Liu, S. Guo, Y. Li, Y. Ma, M. Liu, Y. He, F. Kang, Dielectric filler-induced hybrid interphase enabling robust solid-state li metal batteries at high areal capacity, Advanced Materials 36 (2024) 2311195. https://doi.org/10.1002/adma.202311195.

[8] Y. Zeng, L. Zhao, J. Zhang, Q. Li, D. Sun, Y. Ren, Y. Tang, G. Jin, H. Wang, La_2 O_3 filler's stabilization of residual solvent in polymer electrolyte for advanced solid-state lithium-metal batteries, Small Science 3 (2023) 2300017. https://doi.org/10.1002/smsc.202300017.

[9] Z. Wang, Y. Hou, S. Li, Z. Xu, X. Zhu, B. Guo, D. Lu, K. Wang, Quasi-solid composite polymer electrolyte-based structural batteries with high ionic conductivity and excellent mechanical properties, Small Structures 5 (2024) 2400050. https://doi.org/10.1002/sstr.202400050.

[10] S. Zheng, Z. Li, L. Chen, Y. Huang, J. Shi, S. Wang, Y. Liu, Y. Liu, Y.-P. Cai, Q. Zheng, MOF-based 3D ion-conducting network enables high-voltage all-solid-state lithium metal batteries at room temperature, ACS Materials Lett. 5 (2023) 1136–1144. https://doi.org/10.1021/acsmaterialslett.3c00077.

[11] G. Lu, H. Wei, C. Shen, F. Zhou, M. Zhang, Y. Chen, H. Jin, J. Li, G. Chen, J. Wang, S. Wang, Bifunctional MOF doped PEO composite electrolyte for long-

life cycle solid lithium ion battery, ACS Appl. Mater. Interfaces 14 (2022) 45476–45483. https://doi.org/10.1021/acsami.2c13613.
[12] J. Zhao, S. Huang, Y. Zhao, C. Cui, Y. Zhang, H. Lin, C. Zhao, W. Dai, Z. Liu, X. Song, P. Cao, Ultra-stable solid-state lithium metal batteries with ferroelectric oxide-enhanced PVDF-based hybrid solid electrolytes, J. Mater. Chem. A 13 (2025) 9347–9356. https://doi.org/10.1039/D4TA08724K.
[13] J. Mi, J. Ma, L. Chen, C. Lai, K. Yang, J. Biao, H. Xia, X. Song, W. Lv, G. Zhong, Y.-B. He, Topology crafting of polyvinylidene difluoride electrolyte creates ultra-long cycling high-voltage lithium metal solid-state batteries, Energy Storage Materials 48 (2022) 375–383. https://doi.org/10.1016/j.ensm.2022.02.048.
[14] J. Li, X. Zhu, Z. Xu, H. Ren, S. Muhammad, H. Yang, B. Luo, M.U. Javed, C. Yu, Y. Zhang, Z. Wang, K. Wang, B. Guo, Dynamic metal-ligand coordinated self-healing polymer electrolytes for lithium-ion batteries: Correlating coordination mechanisms with electrochemical properties, Adv Funct Materials (2025). https://doi.org/10.1002/adfm.202510177.
[15] L. Gao, B. Tang, H. Jiang, Z. Xie, J. Wei, Z. Zhou, Fiber-reinforced composite polymer electrolytes for solid-state lithium batteries, Advanced Sustainable Systems 6 (2022) 2100389. https://doi.org/10.1002/adsu.202100389.
[16] H. Yang, Z. Wang, X. Zhu, Z. Xu, J. Li, B. Luo, B. Guo, K. Wang, Enabling enhanced ion transport in PVDF-HFP electrolytes by engineering local dielectric microenvironments with dual-functional SrTiO3/LLZTO fillers, Chemical Engineering Journal 525 (2025) 170151. https://doi.org/10.1016/j.cej.2025.170151.